applied optics

Toward an operational stray light correction for the Landsat 8 Thermal Infrared Sensor

Matthew Montanaro,[1,*] Aaron Gerace,[1] and Scott Rohrbach[2]

[1]Rochester Institute of Technology, 54 Lomb Memorial Drive, Rochester, New York 14623, USA
[2]NASA Goddard Space Flight Center, 8800 Greenbelt Road, Greenbelt, Maryland 20771, USA
*Corresponding author: montanaro@cis.rit.edu

Received 21 January 2015; revised 6 March 2015; accepted 14 March 2015; posted 16 March 2015 (Doc. ID 233075); published 22 April 2015

The Thermal Infrared Sensor (TIRS) onboard Landsat 8 was tasked with continuing thermal band measurements of Earth as part of the Landsat program. From first light in early 2013, there were obvious indications, such as nonuniform banding and varying absolute calibration errors, that stray light was contaminating the thermal image data collected from the instrument. Stray light in this case refers to unwanted radiance from outside the field-of-view entering the optical system and being recorded by the focal plane. Standard calibration techniques used to flat-field and radiometrically correct the data were not sufficient to adjust the image products to within the accuracy that the Landsat community has come to expect. The development of an operational technique to remove the effects of the stray light in the TIRS data has become a high priority. A methodology is presented that makes use of a stray light optical model developed for the instrument along with knowledge of the out-of-field area surrounding the TIRS earth scene. Two versions of the algorithm are proposed in which one method utilizes near-coincident image data from an external sensor while another novel method is proposed that makes use of TIRS image data itself without the need for external data. Preliminary results of the algorithm indicate that banding artifacts due to stray light are significantly reduced when the methods are applied. Additionally, initial absolute calibration error estimates of over 9K are reduced to within 2K when applying the correction methods. Although both variations of the proposed algorithm have significantly reduced the stray light effects, the fact that the latter method utilizing TIRS image data itself does not rely on any external data is a significant advantage toward the development of an operational stray light correction solution. Ongoing work is focused on operationalizing the algorithm and identifying and quantifying potential sources of error when applying the method. © 2015 Optical Society of America

OCIS codes: (290.2648) Stray light; (290.2745) Ghost reflections; (280.4991) Passive remote sensing; (110.3080) Infrared imaging.

http://dx.doi.org/10.1364/AO.54.003963

1. INTRODUCTION

The Thermal Infrared Sensor (TIRS) was included as part of the imaging payload of the Landsat 8 mission launched in February 2013. Shortly after the instrument checkout and commissioning, several anomalies were observed in the TIRS image data that could not be corrected through conventional calibration methods [1]. Most notably, banding within and between the focal plane arrays was observed, the structure of which varied scene-to-scene, impacting the uniformity of the image product. Additionally, comparison of TIRS image-derived radiances with coincident truth measurements showed a season-varying absolute radiance error [2]. These effects have since been attributed to stray light from the out-of-field area of the instrument adding an unwanted nonuniform ghost signal across the focal plane arrays [3].

This paper documents the progress toward the development of an operational correction for the stray light effects in TIRS imagery. Special data acquisitions of the moon by the instrument confirmed the stray light artifacts. Subsequent optical modeling, which verified the source of the stray light, has led to the development of stray light source-map information for each detector. Two correction methodologies utilizing these stray light maps along with knowledge of the out-of-field content are presented here.

A. Instrument Overview

A cursory overview of the instrument is necessary to define terms and geometry for the subsequent discussion. TIRS collects image data of Earth utilizing a push-broom architecture in two spectral channels. The instrument consists of three focal plane detector arrays known as sensor chip assemblies (SCAs) as shown in Fig. 1. Each array consists of 512 rows by 640 columns of detectors. Spectral interference filters are placed over selected areas of the arrays to provide one spectral channel sensitive between 10.6 and 11.2 μm (Landsat 8 band 10) and another channel sensitive between 11.5 and 12.5 μm (Landsat

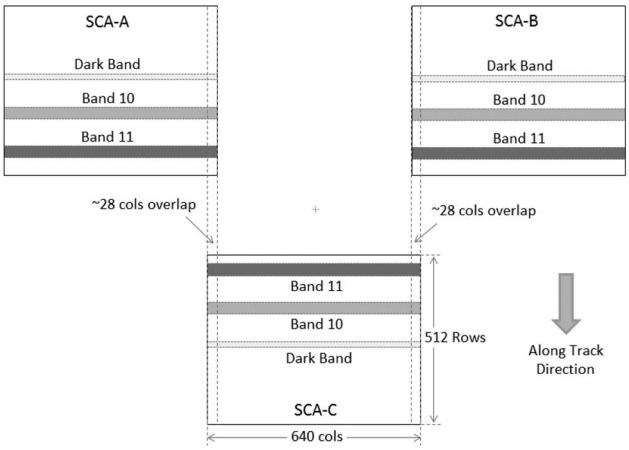

Fig. 1. TIRS focal plane consists of three sensor chip assemblies (labeled SCA-A through SCA-C). Spectral filters are used to produce rows of detectors on each array for the two spectral channels (band 10 and band 11) for the push-broom configuration of the instrument. There are a total of 1920 detectors per band across the three arrays to cover the 15° across track field-of-view [1].

8 band 11). Areas of the arrays that are not spectrally filtered are masked off. The TIRS optical system consists of a four-element refractive telescope that is secured into a passively-cooled optical structure. A flat mirror known as the scene select mechanism is positioned in front of the telescope allowing the focal plane to view Earth (nadir), an internal blackbody source, or a port that views deep space for calibration purposes [1,4,5].

The TIRS image product is constructed from a single combined row from each spectral filter region on each array. Data from the three arrays are merged to produce a 185 km ground swath (15° field-of-view). The image data are processed at the United States Geological Survey (USGS) Earth Resources Observation and Science (EROS) data center and released to the public as standard Worldwide Reference System 2 (WRS-2) scenes [6,7].

The on-orbit performance of the instrument is continually monitored. Data from the onboard calibration sources are obtained every orbit, and instrument telemetry is constantly tracked. All data points indicate that TIRS is electrically and thermally stable and the response to the onboard sources do not vary significantly over time [8].

2. OVERVIEW OF STRAY LIGHT EFFECTS

The conclusion that TIRS suffers from a stray light problem was derived from artifacts observed in Earth imagery as well as from special data collections where the moon was used as a controlled out-of-field source. The investigation that led to the discovery of the stray light issue is summarized here and provided in further detail in Montanaro *et al.* [3].

A. Artifacts in TIRS Image Data

Certain artifacts were observed in the TIRS image data after the first months of on-orbit operation. These effects fall into two main categories: nonuniform banding and seasonal variations in absolute calibration errors. Both represent undesirable behavior of the instrument and pose significant challenges for calibration efforts.

1. Banding

The low frequency variation in the across-track direction in image data from scenes that are expected to be uniform is known as banding. The banding structure that appears in certain TIRS images manifests itself both as a sudden shift in value on either side of an SCA boundary and as a slow variation in signal within an SCA. The examples shown in Fig. 2 demonstrate both of these banding effects. The difference in radiance values between the center and the right-hand array in Fig. 2 (left) is approximately 4.5%. The Red Sea image in Fig. 2 (right) is particularly revealing in that the banding seems to vary with line number (i.e., vary with each push-broom frame). The ratio of image radiance values straddling the boundary between the center and the right-hand arrays varies by approximately 2.5% in the along-track direction from the north end of the scene to the south end. Although only two examples of banding are shown in Fig. 2, a variety of other scenes exhibit similar banding structure whose magnitude and spatial structure vary from scene to scene.

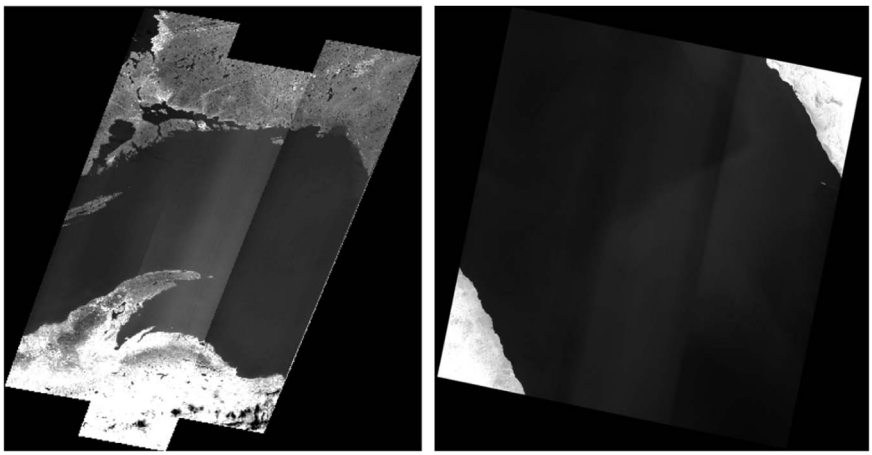

Fig. 2. Two examples of banding artifacts in TIRS band 11 imagery: Lake Superior (left) and Red Sea (right). The nonuniform signal is mostly evident at the boundaries between the three focal plane arrays (refer to Fig. 1).

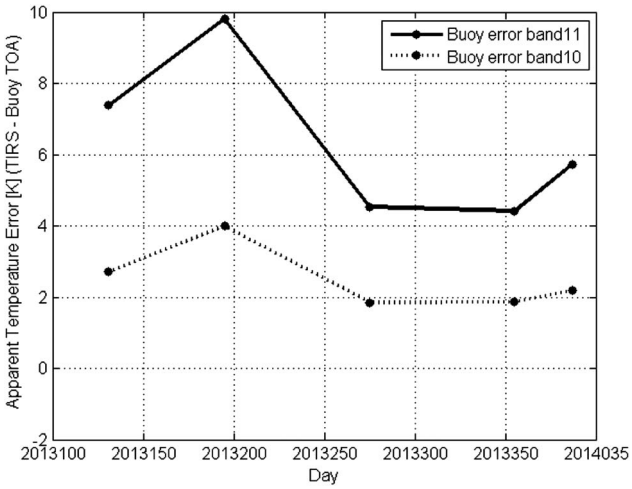

Fig. 3. Absolute radiometric calibration error between TIRS image-derived radiance and the top-of-atmosphere (TOA) buoy measurements from Lake Tahoe for band 10 (dotted line) and band 11 (solid line).

2. Absolute Radiometric Calibration Error

TIRS utilizes *in situ* measurements as an absolute radiometric calibration reference. Buoys in bodies of water such as Lake Tahoe, California directly measure the temperature of the water. Radiative transfer models can be used to derive at-sensor radiance for comparison to satellite radiance data. Water bodies are ideal for this application as the emissivity of water is stable and well characterized in the thermal infrared, which greatly simplifies radiometric modeling [9]. The top-of-atmosphere (TOA) radiance in the TIRS spectral channels from these bodies of water is derived from the lake temperature and from models of the atmosphere at the time of image acquisition [10]. The difference between the TIRS image-derived radiance and the computed TOA radiance of the water body represents the absolute radiometric calibration error for the instrument [9]. This approach has been used to calibrate the thermal bands of Landsat 5 and 7 to within 0.7K [11].

Buoy TOA radiances have been continuously compared to TIRS image data since the activation of the instrument in early 2013 [2]. Although buoy measurements for a variety of water bodies have been monitored, a select sample of measurements from the Lake Tahoe buoys are illustrated in Fig. 3. The five TOA radiances for the scenes were provided by Simon Hook at NASA Jet Propulsion Laboratory. The difference between the TIRS-derived radiance and the TOA buoy radiance (expressed as an apparent temperature difference) indicates a seasonal effect in which the calibration error is larger during the summer and smaller during the winter. The data indicate that the issue is more complicated than a simple bias error that affects the absolute calibration. A complete treatment of the absolute radiometric calibration for TIRS is available in Barsi *et al.* [2].

B. Stray Light Hypothesis

The image artifacts presented in Section 2.A are not only an annoyance visually but also limit the scientific utility of the TIRS data. The banding artifacts have been shown to vary from scene to scene and can be in excess of 8% [3]. The magnitude and the spatial shape of the banding seem to be dependent on out-of-field scene content. In addition, the magnitude and shape of the banding may vary within a scene itself (e.g., Fig. 2, right). The fact that the banding changes for each image line (i.e., push-broom frame) indicates that an issue other than standard detector-to-detector uniformity differences is at play, i.e., a standard flat-fielding approach to correct the banding would not correct the problem.

The varying absolute calibration error is another indication of a more complicated issue with the instrument. The TIRS image data always report a higher radiance value than *in situ* measurements derived from buoys as described in Section 2.A.2. Furthermore, this error varies with season so that the error has a larger magnitude during the summer and a smaller magnitude during the winter. The error between TIRS and *in situ* measurements seem to be proportional to the average out-of-field temperature.

The evidence presented here suggests that an out-of-field radiance (stray light) is adding a spatially varying signal to the focal plane (ghosting). This stray light effect would explain the artifacts seen in the TIRS image data. The absolute calibration error is higher in the summer since the surrounding scene area is hotter and would therefore contribute a higher magnitude of stray light signals on the detectors. The varying out-of-field content would produce different magnitudes of the stray light signal across the focal plane so that some detectors would report a higher signal than others, which visually appears as banding on the arrays.

C. Confirmation of Stray Light

The stray light suspicion was confirmed through special data acquisitions of the moon. The moon is an excellent concentrated source that can be systematically scanned throughout the TIRS out-of-field area (the moon is approximately 0.5° in diameter as compared to the 15° field-of-view for TIRS). The Landsat 8 observatory is agile enough to slew and point TIRS to the desired locations in space to provide the appropriate geometry between the moon and the TIRS optical boresight [3].

The intention of the lunar scans was to not directly image the moon; therefore the focal plane should detect no signal. In other words, only radiance from a detector's instantaneous field-of-view should produce a signal on that detector. If a signal is detected from the out-of-field source, then the magnitude of that signal can be recorded along with the line-of-sight information for the particular source (lunar) position. Figure 4 demonstrates this concept with actual TIRS image data from a lunar scan. For this particular frame, the position of the moon outside the field-of-view is indicated relative to the location of the focal plane detectors. The ghost signal is clearly seen on both bands on SCA-A. The stray light from this lunar position affects multiple individual detectors. The magnitude of the ghost signal is relative to the lunar signal when directly imaged by the focal plane.

The stray light magnitude and the lunar position information for every detector can be assembled into a form that is useful for algorithm development. For a particular detector, a list of all the lunar positions that contributed a ghost signal to that detector represents a map of the out-of-field stray light

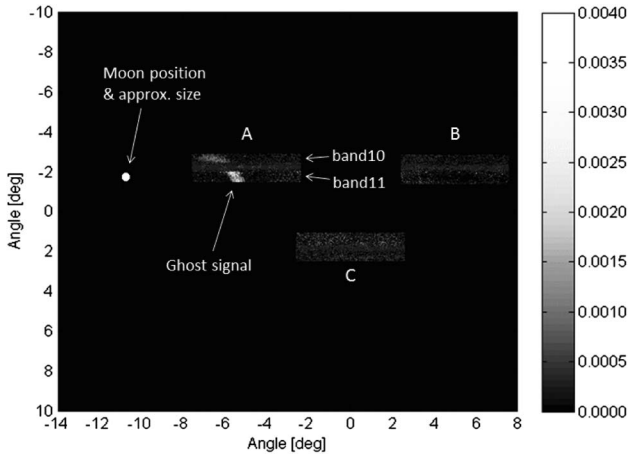

Fig. 4. Diagram demonstrating the processed lunar scan data as the focal plane arrays are spatially oriented. The position of the moon relative to the arrays is indicated (the position angles are relative to the optical boresight). For this particular lunar position, a ghost signal appears on both bands in array A as indicated. The contrast scale indicates the fraction of the directly-imaged lunar signal [3].

locations for the detector. This detector stray light map is analogous to a point-spread function (PSF) that provides the direction of the stray light source and the relative magnitude of the signal from that direction. Two examples of this dataset are illustrated in Fig. 5. The maps are sparsely populated since the moon was not scanned through every location in the out-of-field area. Despite this limitation, the lunar data is very useful to establish a sense of how far off-axis and the extent of the stray light source locations for every detector. The stray light source is approximately 10° to 15° from the optical boresight of the instrument. Also noteworthy is that the stray light affects each detector differently (see Section 3.B).

3. OPTICAL STRAY LIGHT MODEL

The lunar scan data represents valuable operational stray light information from the as-built instrument. The dataset was provided to the Optics group at NASA Goddard Space Flight Center in order to calibrate a TIRS optical stray light model. The purpose of the model was to develop more densely sampled stray light maps for each detector and to identify potential causes of the stray light in the optical system.

A. Model Description

A stray light model of the TIRS optical system, including the scene select mirror, telescope, spectral filter assembly, and the focal plane assembly, was built in the FRED Optical Engineering software. The optical elements were taken from the ZEMAX optical design at operational temperature, approximately 185K for the telescope. The hardware elements were designed based on the TIRS computer aided drafting model and were scaled from room temperature to operational temperature [12].

All internal hardware elements were initially set to have a 90% specular reflectivity as a starting point. The reflectance of each type of surface (black anodized aluminum, machined Meldin, ground edges of optical elements, etc.) was then tuned until the modeled stray light signature matched the observed lunar data at five different field points across the field-of-view from the series of lunar scans (recall Section 2.C). This tuning showed that the black anodized surfaces do not contribute at a measurable level to the stray light signal and that only the reflectance from the thin, Meldin spacer ring immediately above the third lens in the telescope is necessary to replicate the

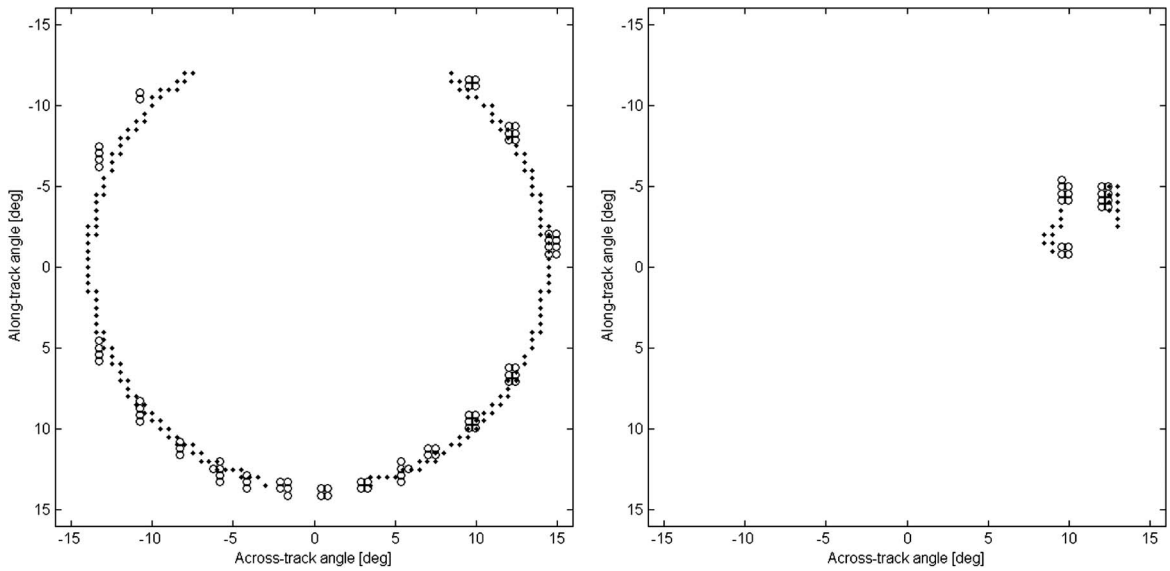

Fig. 5. Graphs of the stray light source locations of two different detectors from array-C (left) and array-B (right) in band 11 based on the optical model (dots) as compared to the lunar scans (circles). Each data point represents a location (an angle in the across-track and along-track direction from the optical boresight) from which a ghost signal was observed for the particular detector. As implied in these diagrams, the stray light sources are different for each detector across the focal plane.

observed signal (see Section 3.C). The Meldin spacer was found to be approximately 100% reflective at the angles and wavelengths for TIRS.

B. Comparison to Lunar Data

Once the optical model was established, it was held fixed (i.e., the physical geometry and optical properties of all surfaces are constant) and a reverse ray trace through the system is performed for each detector. One million rays were cast outward from each detector position in random directions within a 40° half-cone angle. For all scattered rays that exited the optical system, their exit directions and intensities were summed into 0.5° bins. A map is thus created for each detector that records the exit direction and relative intensity of each ray through the optical system. A ray that did not make it through the system would have a value of zero in the map. Values above zero would indicate the relative strength of the ray in the particular direction. A ray with double the value of another ray would mean that the first direction would contribute twice as much stray light on that detector than the second direction. These modeled measurements are similar to the lunar measurements in which the direction and relative strength of the stray light signal is recorded. As with the lunar data, the optical model yields a map, or point-spread function, for each detector. Unlike the lunar measurements however, the optical stray light maps are densely populated since a sufficient number of rays can be cast in the model to obtain a complete stray light mapping. A comparison of the lunar and the optical model stray light maps for two detectors are demonstrated in Fig. 5 where the solid dots represent stray light sources derived from the optical model and the open circles indicate stray light sources observed during the lunar scans. The agreement with the lunar data offers confidence in the optical stray light model and in the resulting stray light maps for each detector.

C. Stray Light Scattering Surface

The optical model allowed for the identification of the primary surface in the optical system that causes the stray light effects. Analysis has shown that the Meldin retaining ring that secures the third lens element into the telescope structure is the primary source of the stray light. The reflectance of this element at thermal infrared wavelengths was underestimated during preflight studies of the optical system. Off-axis rays are able to reach the focal plane via reflection off this ring surface as illustrated in Fig. 6.

To correct for the issue on future instrument builds, the diameter of the retaining ring may be enlarged to prevent stray reflections from the surface from reaching the focal plane. Similarly, a small baffle may be placed in front of the third lens element in order to block off-axis view angles from reaching the retaining ring. These recommendations will be incorporated into any future designs of similar instruments.

4. STRAY LIGHT CORRECTION METHODOLOGIES

The effect of the stray light in TIRS will always add a varying nonuniform ghost signal to the focal plane detectors. Qualitatively, the total radiation incident on a given detector

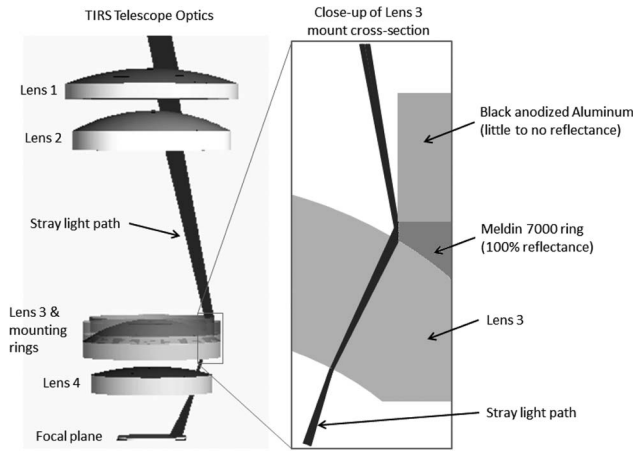

Fig. 6. Illustration of the TIRS telescope and focal plane (left). The primary source of the stray light in the TIRS optical system is the Meldin retaining ring for the third lens element (highlighted at right).

is due to the summation of the direct incoming radiation from the detector's instantaneous field-of-view (IFOV) and of the out-of-field ghost signal. The ghost signal is the summation of all stray light source radiances visible by that detector, weighted by the strength of the scattering in the particular direction. Quantitatively, this can be expressed as

$$\begin{aligned} Total\ signal_j &= Direct_j + Ghost_j \\ &= Direct_j + f_j\{\Sigma_i[w_{j,i} \cdot L(\theta_{j,i})]\}, \end{aligned} \quad (1)$$

where L is the out-of-field radiance in the θ_i direction for detector j, $w_{j,i}$ is the weight of the ith direction derived from the optical model for detector j, and f_j indicates that there is a functional relationship between the actual ghost signal observed by detector j and the integrated radiance from the out-of-field. Equation (1) indicates that the ghost signal depends on knowledge of both the stray light source directions and the out-of-field radiance surrounding the scene of interest. To develop a stray light removal algorithm, the optical stray light model maps provide knowledge of the stray light source directions and weighting functions described in Eq. (1). If knowledge of the out-of-field radiance can be obtained, i.e., $L(\theta_i)$, then the integrated ghost signal can be determined and used in a methodology to remove signal from detector j in the image data.

A. Obtaining Out-of-field Radiance

Two methods to acquire or predict the out-of-field radiance per scene are suggested here. Both methods rely on the same basic concept to calculate the magnitude of the stray light signal on each detector.

1. Out-of-field Radiance from an External Sensor

The first method to obtain knowledge of the out-of-field area is to acquire wide-field thermal infrared image data coincident with the TIRS data acquisition. In this case, near-coincident knowledge of the out-of-field radiance can be obtained via the wide-field data.

Meteorological sensors in geostationary earth orbit can be utilized for wide-field thermal band data. Over the Americas,

Geostationary Operational Environmental Satellite (GOES) thermal image data are obtained every 15 minutes and can provide the necessary out-of-field data for TIRS [13]. Similar platforms exist for other parts of the world (e.g., Meteosat for Europe and Africa; Himawari over eastern Asia; etc. [14,15]). While weather satellites offer a convenient source of out-of-field thermal infrared data, their spectral channels likely differ from those on the TIRS, which is a land-based imager. Therefore, the thermal band data should be adjusted to the TIRS spectral channel if the band shapes of the two sensors are not equivalent [11]. Additionally, data from sensors located in geostationary orbits are not useful for TIRS scenes of high latitudes. In these cases, data from polar orbiting sensors such as Moderate Resolution Imaging Spectroradiometer (MODIS) may be utilized for TIRS out-of-field information. The method developed here uses GOES/Imager thermal data (band 4) as an example but the same technique may be applied to other thermal sensors. A variety of external datasets will be necessary to achieve global coverage of the out-of-field information for all TIRS scenes.

The objective is to sample the out-of-field radiance (i.e., the external sensor data) using the stray light map information per detector as described in the summation term in Eq. (1). Referring to Fig. 7 for a particular detector, the stray light map line-of-sight (LOS) vectors are utilized to determine which locations in the external sensor data must be sampled and weighted to derive the stray light signal on the detector. The LOS vectors are projected onto Earth and expressed as a series of latitude/longitude pairs. If the external sensor data contains geolocation data as well, then the nearest latitude/longitude pixel in the external data can be found for each stray light vector latitude/longitude. These locations are weighted and summed accordingly via Eq. (1). Since the external thermal data covers the complete out-of-field area of TIRS, radiance for all stray light source locations can be obtained.

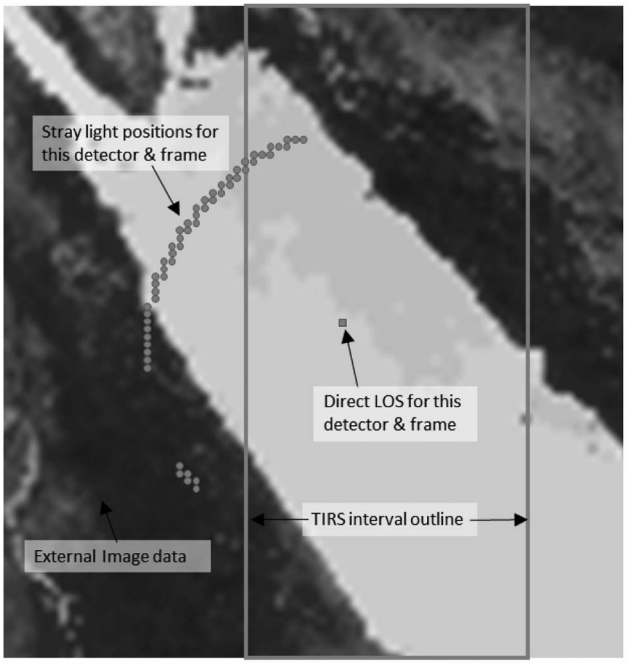

Fig. 7. Projection of the stray light LOS vectors onto wide-field image data from an external sensor (MODIS in this example) for one detector (for one push-broom frame). A similar projection is performed for every other frame and likewise for every other detector. The radiance of the nearest pixel in the wide-field data to each stray light vector is sampled.

2. Out-of-field Radiance from TIRS Data

A handful of sensors have been suggested in the previous section that may be used to achieve global coverage of near-coincident data to provide knowledge of the out-of-field radiance contributing to the stray light in TIRS. However, processing near-coincident wide-field thermal infrared image data anywhere on the globe would be operationally challenging. Therefore, there is a strong desire from an operational ground processing standpoint to obtain these out-of-field data as quickly as possible to calculate the necessary correction. Since Landsat 8 has routinely been collecting 650+ scenes per day, a significant and undesired processing backlog would result should external sensor data need to be ingested as part of the standard processing and product generation system.

An alternative method to obtain the coincident out-of-field radiance is preferred. The technique proposed in this work involves utilizing TIRS image data itself as a surrogate for the out-of-field radiance. The method takes advantage of the fact that TIRS collects image data along a WRS-2 path interval that consists of many TIRS WRS-2 scenes. Recall from Section 2.C that the stray light sources are roughly 15° in either direction from the scene. Referring to Fig. 8, for any given scene

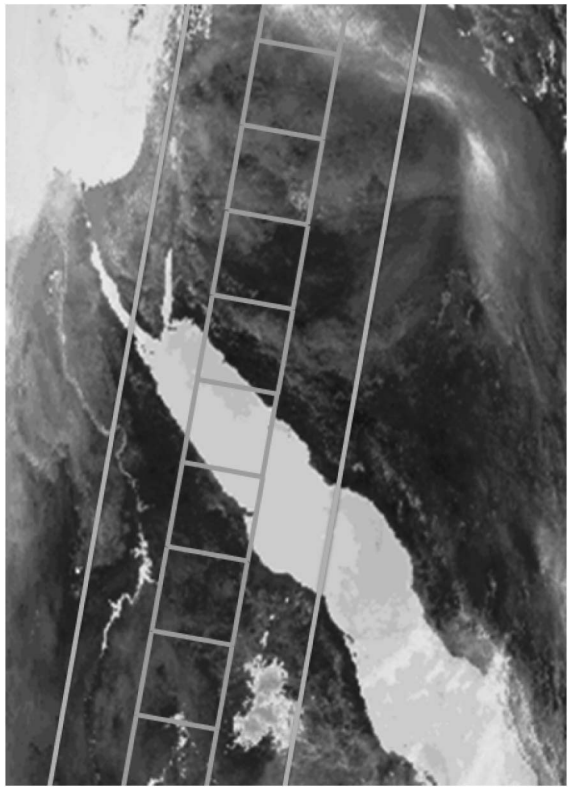

Fig. 8. Context image for TIRS out-of-field content. The squares outline the TIRS WRS-2 scenes for the path interval while the parallel lines indicate the approximate stray light source area on either side of the TIRS interval.

(illustrated with the squares) on an orbital path there are TIRS data available for the preceding and for the following scene. These data provide the out-of-field information in the along-track direction. Since there is not coincident TIRS image data for the out-of-field area in the across-track direction (on either side of the WRS-2 path interval), a substitute is needed. The assumption is made that for any given image line (push-broom frame), the radiance at the edge of the image is roughly the same as the radiance immediately outside the path. Therefore, the pixel values on the edge of the scene image are used as a surrogate for the radiances on either side of the WRS-2 path.

The sampling procedure for this technique is the same as for the method described in Section 4.A.1, with the exception that the sampling is performed on the TIRS interval data itself instead of on external sensor data. Recall that for a particular detector, the stray light map line-of-sight vectors are used to determine locations in the external sensor data to sample and weight via Eq. (1). As before, the stray light LOS vectors are expressed as latitude/longitude pairs. In this method (see Fig. 9) for any stray light vectors that happen to fall within the WRS-2 path where TIRS image data was recorded, the sampling algorithm will simply find the TIRS pixel nearest to that stray light vector. For stray light vectors that fall outside the WRS-2 path where there is not TIRS image data, the sampling algorithm will again find the nearest TIRS pixel. However, for this situation the nearest pixel will be at the edge of the data interval. This is acceptable under the assumption that the pixels near the interval edge are a reasonable surrogate for radiances outside the scene, in general.

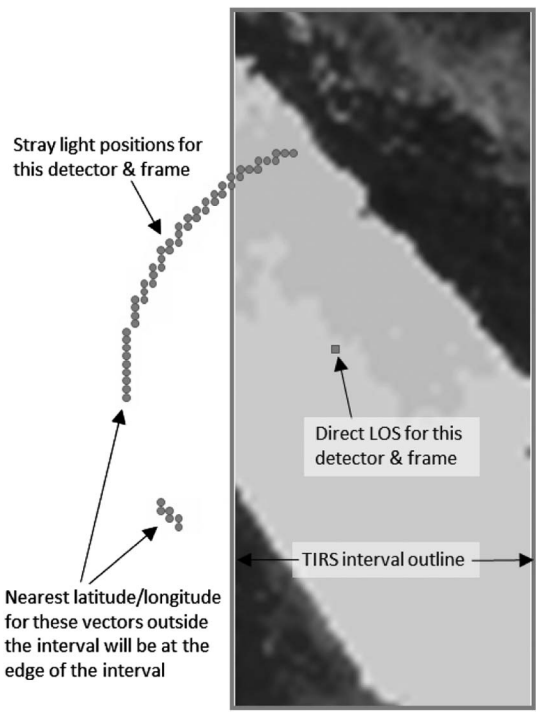

Fig. 9. Projection of the stray light LOS vectors onto TIRS image data obtained from the current WRS-2 path interval of Earth for one detector (for one push-broom frame). Stray light vectors that fall within the interval are able to sample the correct radiances in the TIRS interval. Stray light vectors that fall outside the interval are forced to sample radiances at the edge of the interval, which serve as a surrogate for the true radiances that would exist at the locations where the stray light vector intersects Earth outside the interval.

A potential issue of this method arises from the fact that the TIRS data is itself contaminated with stray light effects and is being used to determine the out-of-field radiance, therefore the predicted out-of-field radiance would always be biased high. However, this effect is minimized due to the regression process between the sampled out-of-field and the actual ghost signal (see Section 4.B.3). Additionally, the total stray light signal on a detector is a few percent of the direct signal from the IFOV so that the effect of using stray light contaminated data is likely negligible.

The primary advantage of this method is that no external wide-field data is necessary. The sampling data required for this technique is automatically available any time TIRS acquires earth imagery since only the TIRS imagery itself is necessary to compute a stray light correction. The primary disadvantage of this method is the assumption that the edge pixels of the TIRS interval are a good representation of the out-of-field content in the across-track direction. The deficiency arises when the edge pixels are of a different material (i.e., a different temperature) than the out-of-field. The areas around the land/water interface in the Red Sea in Fig. 9 are examples of this case where the out-of-field may be land but the nearest edge is water, or vice versa. Similarly this method will not be able to account for clouds off-scene if those same clouds are not also present on the edge of the TIRS interval. The impact of the primary assumption that the edge pixels can be used as an out-of-field source on the accuracy of the removal process remains an area of ongoing research.

B. Stray Light Removal Algorithm

Recalling Eq. (1), the crux of the stray light removal method proposed here is that a functional relationship exists between the observed ghost signal and the integrated out-of-field radiance for each detector, i.e.,

$$Ghost\ signal_j = f_j\{\Sigma_i[w_{j,i} \cdot L(\theta_{j,i})]\}. \tag{2}$$

1. Deriving the Observed Ghost Signal

The ghost signal from Eq. (2) can be derived for each detector by differencing TIRS image data with a known TOA radiance signal in the TIRS spectral channel. A way to estimate the actual TOA signal for every detector is to utilize the MODIS sea surface temperature (SST) product along with atmospheric knowledge at the time of TIRS image acquisition [16,17]. The temperature product is useful for this application since the emissivity of water is well known in the thermal infrared; therefore, modeling TOA radiance is trivial. Additionally, due to its large thermal capacity, the temperature of deep ocean water slowly varies throughout the day so using MODIS data that is nearly coincident with TIRS is sufficient to estimate TOA radiance. Once the TIRS and modeled TOA MODIS image data are spatially registered to each other, the calculated ghost signal is simply the difference between the TIRS and MODIS radiances for fully resolved water pixels. Equation (2) then becomes

$$(L_{\mathrm{TIRS}} - L_{\mathrm{MODIS}})_j = f_j\{\Sigma_i[w_{j,i} \cdot L(\theta_{j,i})]\}. \tag{3}$$

Five TIRS datasets collected over North America were obtained along with the MODIS SST product close in time to the TIRS scenes. The scenes were chosen due to the abundance of water pixels imaged by each detector and due to the large temperature range observed in the water bodies. These considerations enabled a sufficiently trained algorithm.

2. Deriving the Out-of-field Radiance

As mentioned previously, the out-of-field radiance, $L(\theta_{j,i})$, can be obtained by utilizing wide-field thermal infrared data from an external sensor; however, it has been proposed to use TIRS image data itself as a surrogate for the out-of-field radiance. In either case, the stray light map LOS information is used to determine the proper radiances to sample. The sampling steps are a computationally intensive process. The detector stray light map information is expressed as an angle relative to the optical boresight. A convenient way to determine the actual locations to sample in either the external image data or the TIRS image data is to project the stray light map LOS vectors onto Earth's surface so that the intersection points can be expressed in latitude and longitude coordinates. The nearest latitude/longitude pixel in the out-of-field data can be found for each stray light vector latitude/longitude (recall Figs. 7 and 9). The projection of the stray light map vectors onto the Earth ellipsoid can be accomplished with the position and attitude information of the Landsat 8 observatory that is provided in the downlinked telemetry. The projection onto the Earth must be calculated for every TIRS image line (i.e., push-broom frame) since the observatory moves an appreciable distance from one frame to another (as designed for a push-broom system to produce the necessary image data). The computational expense stems from performing this projection and sampling of all stray light vectors for every TIRS detector (1920 per band) and for every TIRS image frame (2100+ per every scene). Note that for band 11, there are over 135,000 stray light vectors per push-broom frame that must be sampled to create the ghost image.

Once the out-of-field radiances are obtained for every stray light LOS vector location, they are weighted according to the stray light map information and summed to obtain a value for the summation in Eq. (3).

3. Deriving the Functional Relationship between Sampled Radiance and Ghost Signal

GOES thermal infrared data that were nearly coincident to the TIRS acquisition (always within 15 minutes) were obtained over the water bodies for the five scenes described above. The detector stray light map PSFs were used to sample the GOES data and determine the integrated (or summed) stray light value for every detector and every image frame. The ghost signal from Section 4.B.1 was then regressed against the corresponding integrated radiance for each detector in an effort to obtain a functional relationship. An example of this is shown in Fig. 10 for one detector. The relationship is nearly linear suggesting that a simple linear regression may be used to relate the ghost signal to the sampled out-of-field radiance. Equation (3) then becomes

$$(L_{\mathrm{TIRS}} - L_{\mathrm{MODIS}})_j = \alpha_j\{\Sigma_i[w_{j,i} \cdot L(\theta_{j,i})]\} + \beta_j, \qquad \textbf{(4)}$$

where α_j and β_j are the linear fit coefficients for each detector j. Note that the linear fit coefficients are different for every detector since the stray light maps are unique to each detector. In addition, as described above, the coefficients are only valid when sampling the specific sensor data in which the out-of-field was sampled (i.e., GOES or TIRS). A new set of coefficients would have to be derived when utilizing wide-field data from a different sensor (although it may be possible to develop an adjustment that would scale each external dataset to allow the same set of regression coefficients to be used universally).

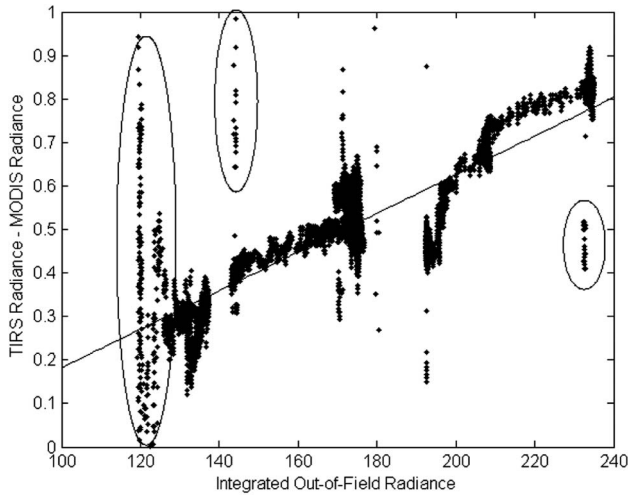

Fig. 10. Relationship between the ghost signal and the summed stray light value for every frame of a given detector. The ghost signal is derived from the difference between TIRS and MODIS radiance for water pixels. The stray light signal for this example was computed by sampling a GOES image utilizing information from the optical stray light model. The data points represent data from all five of the test scenes used to derive the relationship. The linear best-fit line is also shown. The circles highlight outliers in the dataset.

4. Filtering the Training Data

The circles shown in Fig. 10 highlight several data points that appear as outliers when a simple linear regression is used to fit the data. To identify the source of these outliers, the ghost signal can be displayed in image form. Figure 11 shows the ghost signal ($L_{\mathrm{TIRS}} - L_{\mathrm{MODIS}}$) for all detectors used to train the data. Upon closer inspection it is evident that filtering the training data is warranted to avoid clouds and temperature variations in the water that may arise from the time difference observed when collecting the MODIS and TIRS data. Moreover, the differing spatial resolutions of the two datasets lead to significant near-shore temperature variations as the land mask inherent to the MODIS SST product does not adequately mask the TIRS land pixels.

The top zoom window in Fig. 11 indicates that TIRS imaged clouds while MODIS (the data were collected several hours later) did not. Using these data in the regression will clearly introduce error to the process when trying to relate ghost signal to integrated out-of-field radiance. The bottom zoom window of Fig. 11 illustrates the impact of differing spatial resolutions and temporal effects as temperature variations in the land and near-shore regions of the training data are apparent. These data need to be masked as well to properly train the algorithm.

The right side of Fig. 11 shows the training data when a rigorous mask is applied to the data. First, a dilation operation

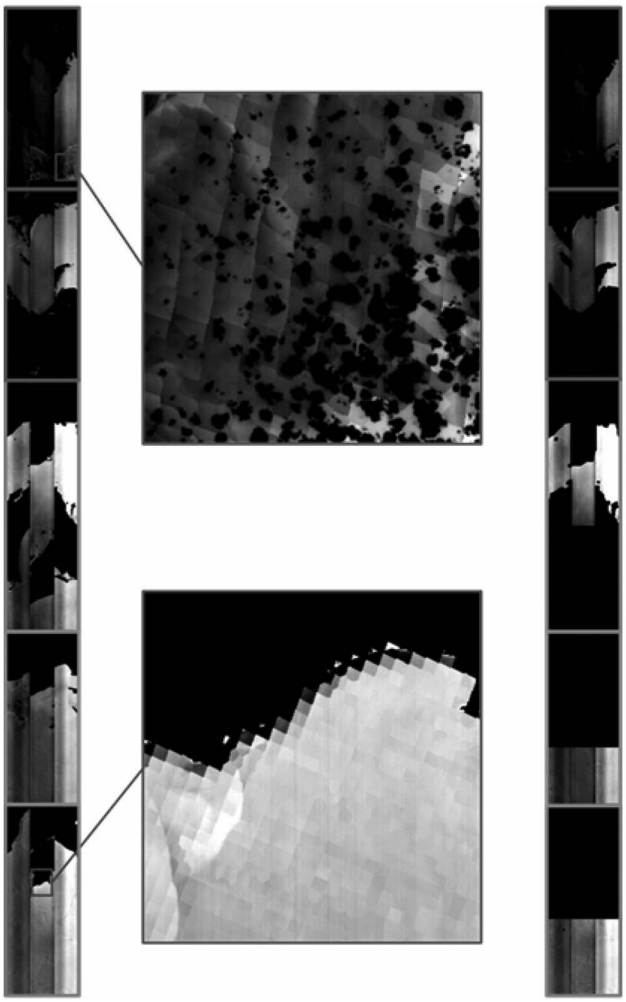

Fig. 11. Five TIRS scenes used to train the stray light correction algorithm (left). Certain data such as clouds (top) and near-shore effects (bottom) must be screened out so as not to affect the regression. The five training scenes after filtering are shown at right.

is applied to the nominal MODIS SST land mask to combat the near-shore artifacts [18]. Second, a manual mask is applied to the data to eliminate near-shore temperature variations suspected to arise from the differing collection times of the two datasets.

Figure 12 shows the regression data from Fig. 10 after a rigorous mask was applied to eliminate the effects due to clouds, differing spatial resolutions, and differing collection times. Since the ghost data of Fig. 11 is presented in an image format, the data for all detectors can be filtered simultaneously and the α and β coefficients determined for each detector.

To evaluate the impact of the filtering process on the estimation of ghost signal, a per-detector average residual was calculated using the training data described thus far. Figure 13 shows the per-detector average residual for both the unfiltered and filtered data for band 11 when both GOES and TIRS were used as an out-of-field data source. Notice that by simply filtering the data to remove cloud, land, and temporal artifacts, the residual error in the correction process for the data presented here can be reduced by nearly a factor of two.

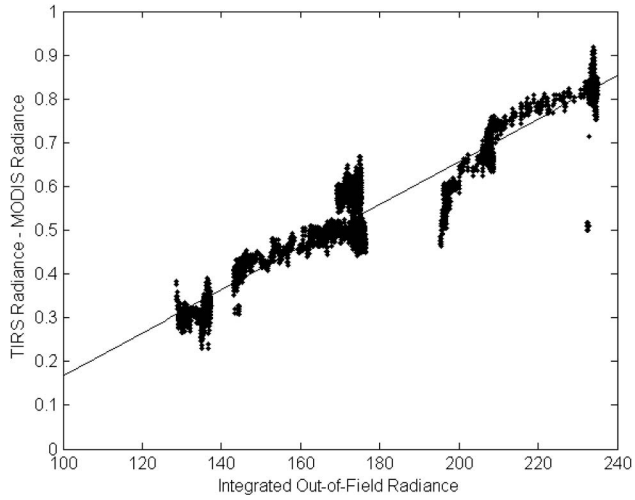

Fig. 12. Regression data from Fig. 10 after filtering of data points to remove the effects of clouds, differing spatial resolutions, and differing collection times. The linear best-fit line is also shown.

5. Algorithm Summary

Once the linear regression coefficients are found for every detector, all required steps are in place to calculate the stray light correction for every detector for any scene. The procedure for every TIRS scene would then involve:

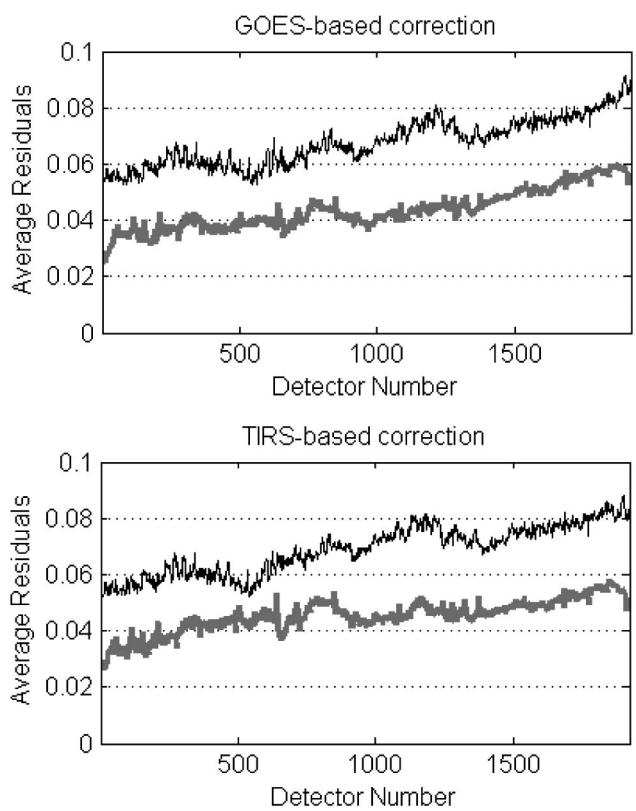

Fig. 13. Linear-fit residuals for unfiltered (black line) versus filtered (gray line) regression data for a single detector in band 11 and comparing the GOES-based correction (top) versus the TIRS-only based correction (bottom). Residuals are in units of spectral radiance.

(1). Obtaining near-coincident wide-field thermal infrared image data (or alternatively, use the TIRS interval data as the out-of-field source).

(2). Obtaining an estimate of the stray light contribution for each TIRS detector by sampling, weighting, and integrating the out-of-field radiance data using the optical stray light model for that detector (for the given frame).

(3). Scaling the stray light value from the sampled wide-field data (or the TIRS data) by the linear regression coefficients to yield the ghost signal for that detector.

(4). Repeating steps (2) and (3) for every image frame and for every detector. The result is a ghost signal value for every pixel in the TIRS scene image.

(5). Subtracting the ghost signal values from the corresponding pixels in the original TIRS radiance data.

5. RESULTS AND COMPARISON OF THE TWO CORRECTION METHODS

The stray light correction method, using both the wide-field GOES data and the TIRS-only interval data, was applied to both band 10 and band 11 for a series of TIRS Earth scenes. Studies in this section were conducted to evaluate the efficiency of the algorithm to remove stray light from the original uncorrected data and to evaluate the assumption that TIRS data can be used as a surrogate for other out-of-field data sources. The stray light correction procedure was applied to scenes used to train the algorithm and then to independent scenes, i.e., scenes not used to train the algorithm.

A. Reduction of Banding Artifacts

Recall that inconsistent array-to-array banding led to the discovery of the TIRS stray light issue. The application of a stray light removal methodology should reduce, if not eliminate altogether, this nonuniform banding. Note that the methodologies presented thus far are strictly stray light removal techniques. They do not replace traditional calibration techniques, i.e., a relative and absolute calibration is still required once the stray light has been adequately removed. Accordingly, results are presented in this section with traditional metrics but are not necessarily an indication of the TIRS final performance.

First, the stray light correction technique was applied to two scenes used to train the algorithm. Path 024 of the WRS-2 crosses Lake Superior between Rows 024 and 026 and represents a colder scene used to generate the regressions (data points to the lower-left in Fig. 12). Both GOES data and TIRS data were used as out-of-field data sources and sampled as described in Secs. 4.A1 and 4.A2, respectively. The appropriate α and β coefficients were applied on a detector-by-detector basis to the resulting sampled integrated radiance to determine the ghost signal to remove from the uncorrected image data [recall Eq. (4)]. The visual results of applying this methodology are shown in Fig. 14. Note that while the banding artifacts are significantly reduced for both out-of-field data sources, banding does still appear near the southern end of the lake. This is an indication that either the source locations and/or the weights derived by the optical model may need to be adjusted to more appropriately sample the out-of-field.

To quantitatively assess the magnitude of the stray light removal, a per-detector average of the TIRS–MODIS difference was obtained over the water for the data shown in Fig. 14 (recall that TOA MODIS was modeled to serve as truth in this study). Figure 15 shows the per-detector root mean squared (RMS) error of TIRS–MODIS both before and after the correction. Notice that, in an absolute sense, the average residual is significantly reduced (especially in band 11) when the stray light correction is applied.

The stray light correction technique was applied to a second scene used to train the algorithm. Path 041 of the WRS-2 crosses the south coast of California between rows 036 and 037. As with Path 024, both GOES data and TIRS data were used as out-of-field data sources and the appropriate α and β coefficients were applied on a detector-by-detector basis to the resulting sampled integrated radiance to determine the ghost signal. Figure 16 shows the results of applying the correction methodology. The algorithm performs extremely well for this scene as the banding is reduced. Figure 17 shows the per-detector RMS difference of TIRS–MODIS both before and after the correction indicating that the average residual is again significantly reduced when the stray light correction is applied.

Finally, the stray light correction technique was applied to a scene not used in the training data. Path 044 of the WRS-2 crosses central California between rows 034 and 036. Again, both GOES data and TIRS data were used as out-of-field data sources and the appropriate α and β coefficients were applied on a detector-by-detector basis to the resulting sampled integrated radiance to determine and subtract the ghost signal from the TIRS image. Figure 18 shows the results of applying the correction methodology. As before, the algorithm performs extremely well as evidenced by the significant reduction in banding and the average over-water residual (see Fig. 19). These examples illustrate the usefullness of the correction methods in reducing the banding artifacts caused by the stray light. Statistics on a large number of corrected scenes are currently being calculated to determine how well the methods perform over a large range of scene temperatures.

B. Absolute Calibration Analysis

Recall from Section 2.A.2 that the absolute radiometric calibration of TIRS based on *in situ* measurements indicates that TIRS always reports a higher temperature than the *in situ* measurements and that the error varies seasonally. The TIRS data of the same dataset shown in Fig. 3 were stray light corrected using both out-of-field data sources and the TOA-derived buoy temperature was compared to the corrected apparent temperature. The results of this analysis are shown in Fig. 20. The method was able to correct the absolute calibration error to within approximately one Kelvin when incorporating external wide-field data for the out-of-field. This method should be the most accurate since it takes the coincident out-of-field radiance into account. The method utilizing only the TIRS path interval data, however, performs almost as well as the wide-field sensor method. The data also show that the seasonal effect of the error is greatly reduced. Similar to the absolute reduction in error when compared to MODIS data, the apparent temperature more closely resembles the buoy-derived temperature after the stray light correction for both out-of-field sources.

The TIRS-only method reduced the absolute calibration error in band 11 to within one Kelvin with the exception of

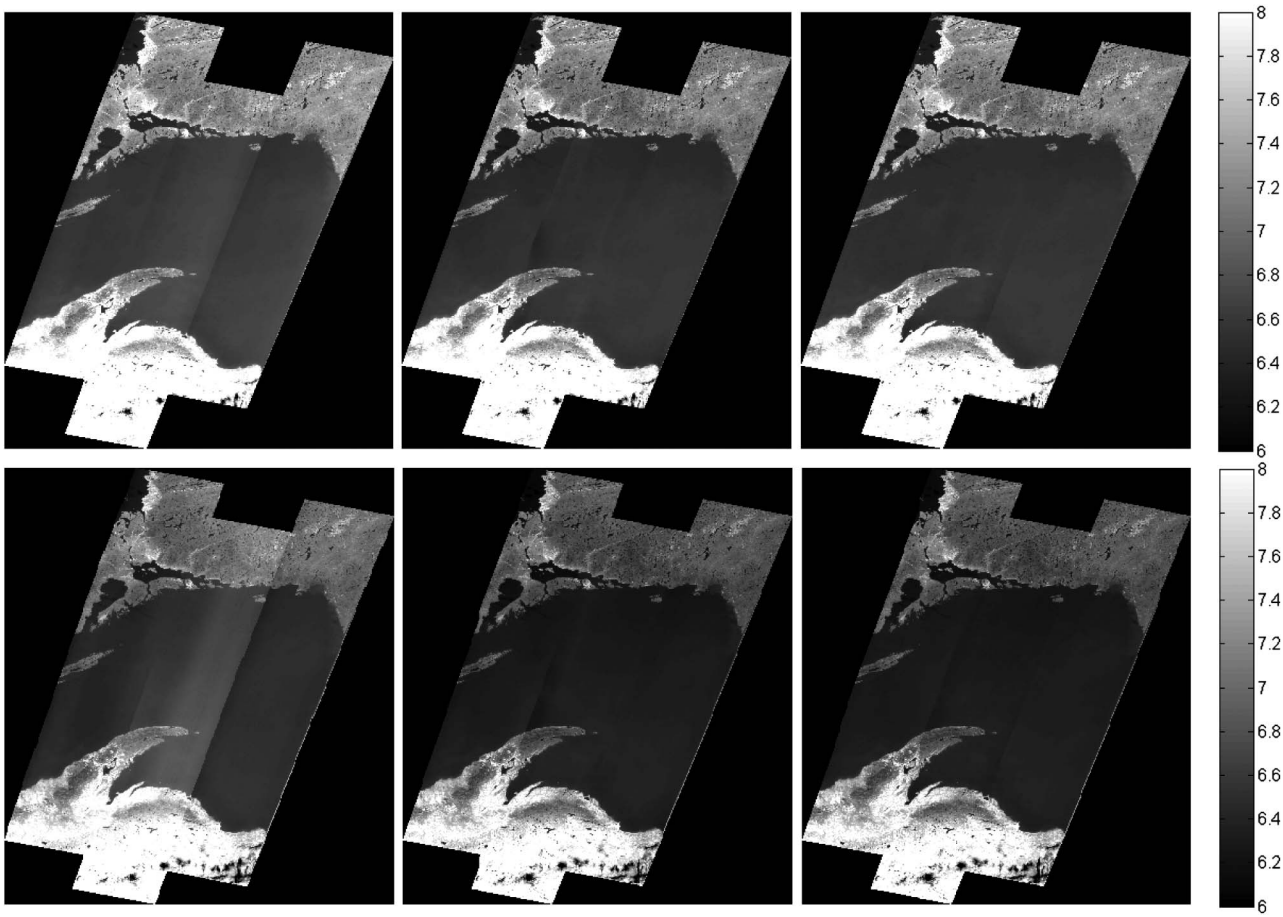

Fig. 14. Comparison of the original TIRS image of WRS-2 scene 024/024-026 from day 2013126 (left) and the results from the two stray light correction methods using GOES wide-field data (center) and using only TIRS data (right) for band 10 (top row) and band 11 (bottom row). The contrast scale is in units of spectral radiance [$W/m^2/sr/\mu m$] and has been stretched to show the banding in the water.

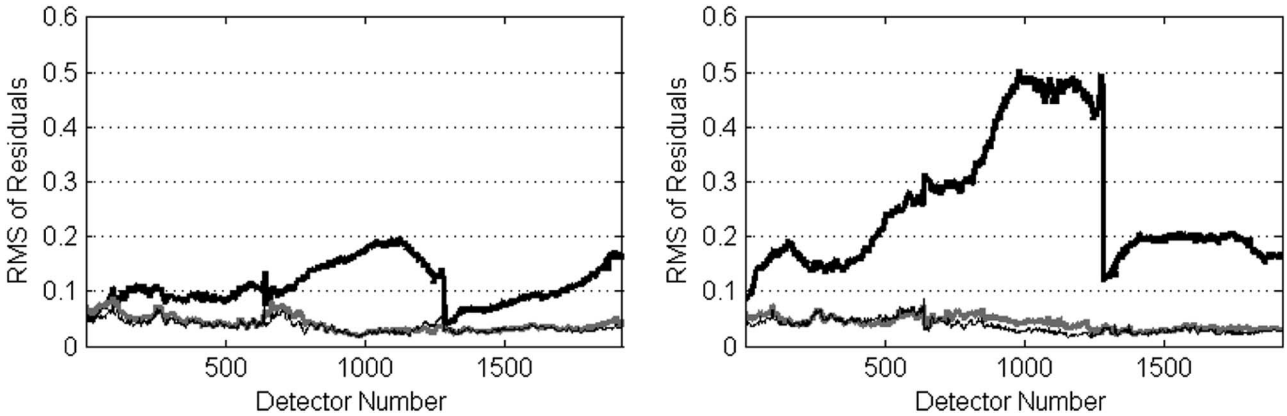

Fig. 15. RMS differences between the MODIS TOA SST radiance and the uncorrected TIRS image (thick black line), the corrected TIRS image using GOES data (gray line), and the corrected TIRS image using only TIRS data (thin black line). The profiles illustrate the residual nonuniformity before and after stray light correction. Band 10 is shown at left and band 11 is shown at right (WRS-2 scene 024/024-026 from day 2013126).

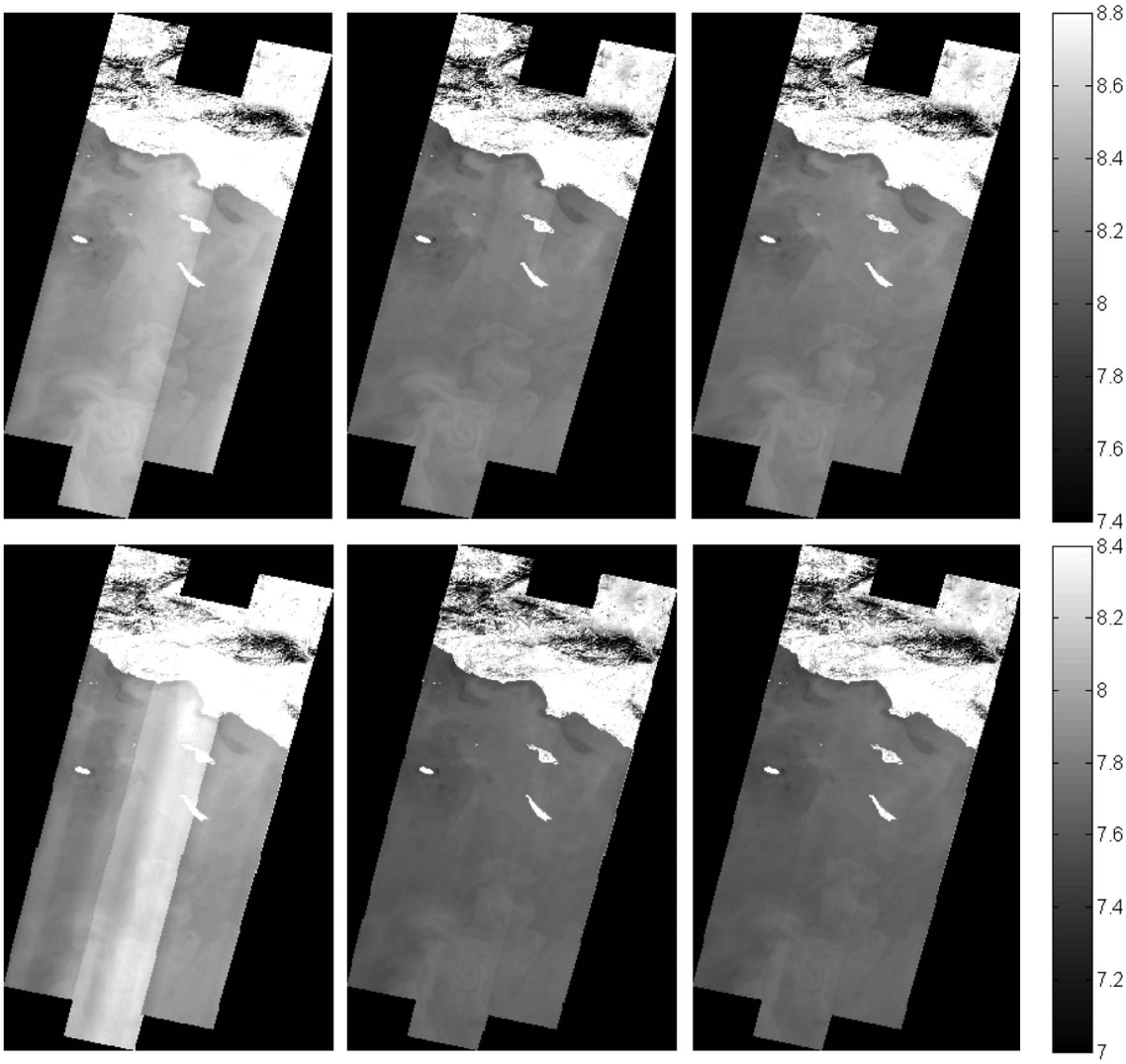

Fig. 16. Comparison of the original TIRS image of WRS-2 scene 041/036-037 from day 2013309 (left) and the results from the two stray light correction methods using GOES wide-field data (center) and using only TIRS data (right) for band 10 (top row) and band 11 (bottom row). The contrast scale is in units of spectral radiance [$W/m^2/sr/\mu m$] and has been stretched to show the banding in the water.

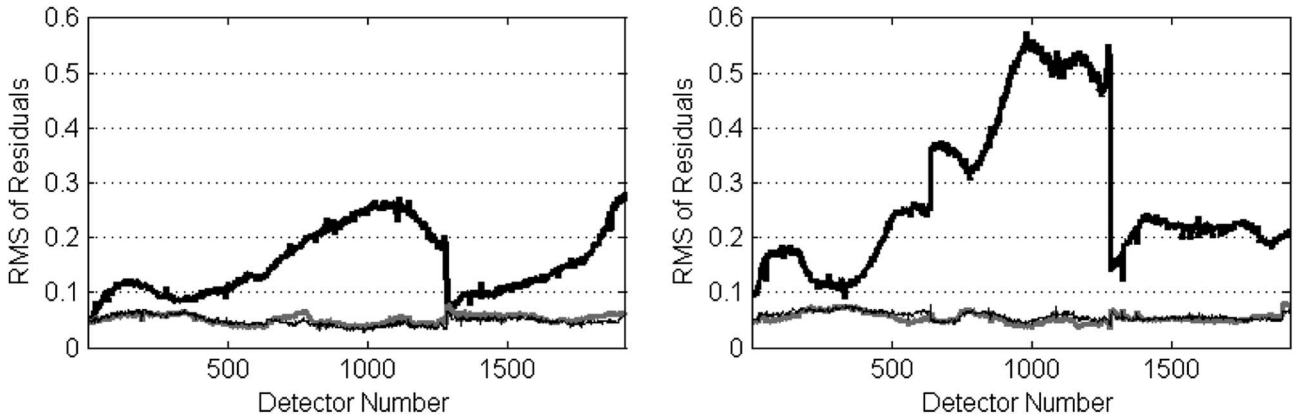

Fig. 17. RMS differences between the MODIS TOA SST radiance and the uncorrected TIRS image (thick black line), the corrected TIRS image using GOES data (gray line), and the corrected TIRS image using only TIRS data (thin black line). The profiles illustrate the residual nonuniformity before and after stray light correction. Band 10 is shown at left and band 11 is shown at right (WRS-2 scene 041/036-037 from day 2013309).

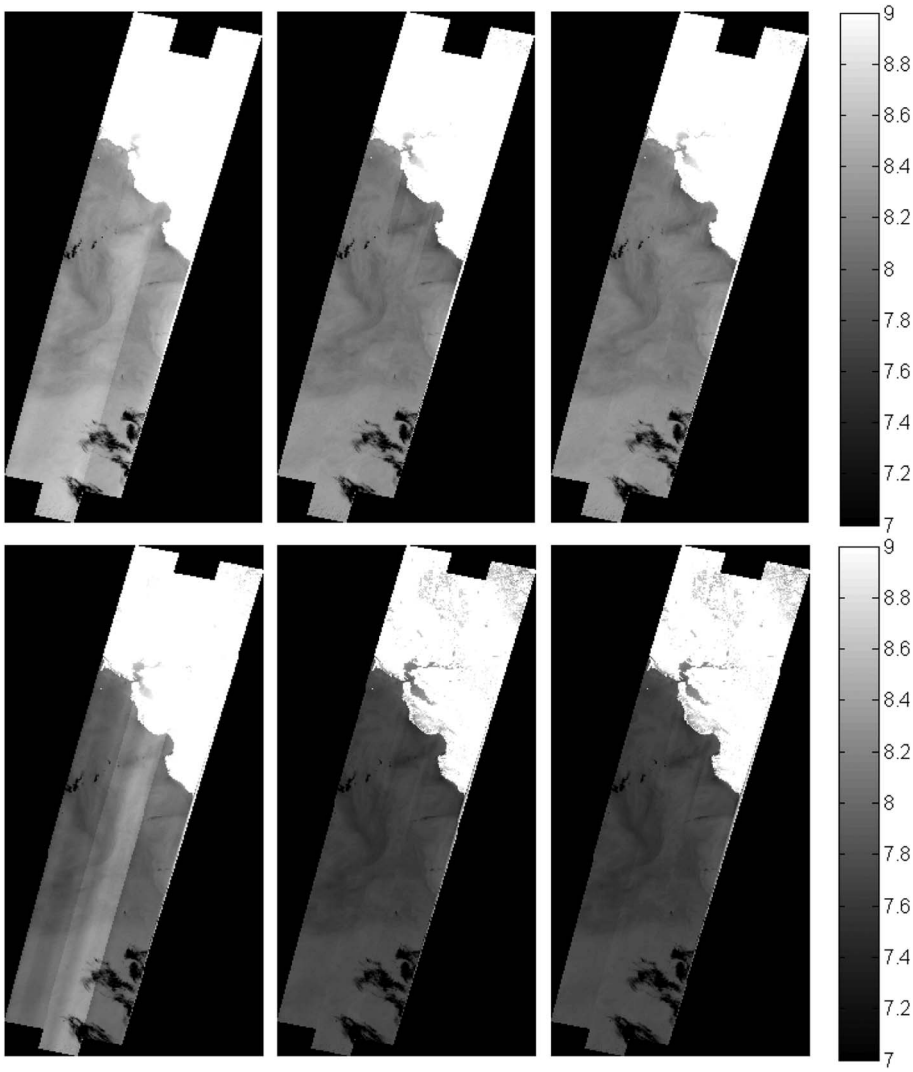

Fig. 18. Comparison of the original TIRS image of WRS-2 scene 044/034-036 from day 2014205 (left) and the results from the two stray light correction methods using GOES wide-field data (center) and using only TIRS data (right) for band 10 (top row) and band 11 (bottom row). The contrast scale is in units of spectral radiance [$W/m^2/sr/\mu m$] and has been stretched to show the banding in the water.

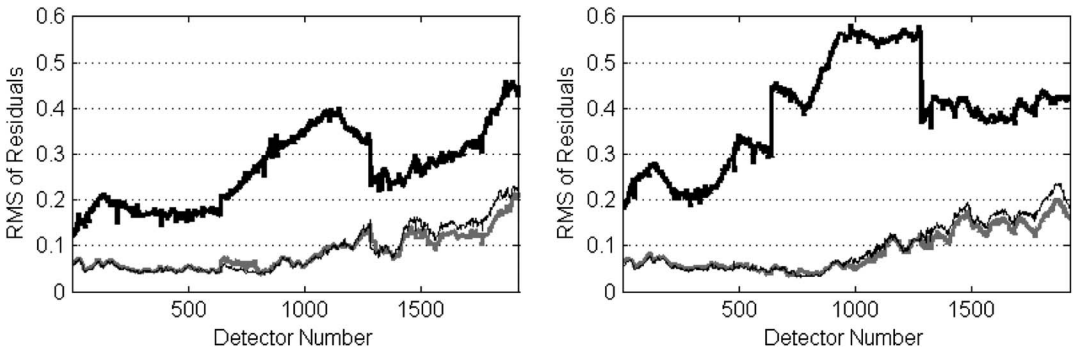

Fig. 19. RMS differences between the MODIS TOA SST radiance and the uncorrected TIRS image (thick black line), the corrected TIRS image using GOES data (gray line), and the corrected TIRS image using only TIRS data (thin black line). The profiles illustrate the residual nonuniformity before and after stray light correction. Band 10 is shown at left and band 11 is shown at right (WRS-2 scene 044/034-036 from day 2014205).

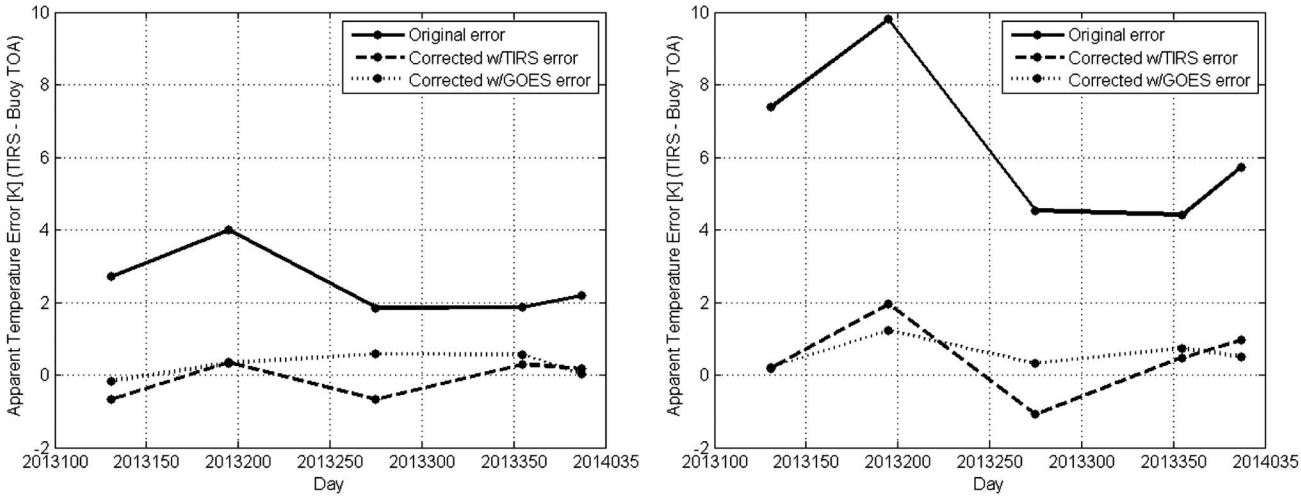

Fig. 20. Absolute radiometric calibration error between TIRS and TOA buoy measurements from Lake Tahoe for band 10 (left) and band 11 (right). The error before stray light correction is shown (solid line) along with the error after correction using the TIRS-only method (dashed line) and using wide-field GOES data (dotted line).

two data points from day 2013195 and day 2013275. To investigate these points further, consider the coincident GOES scenes for each of the TIRS Lake Tahoe scenes in Fig. 21. The GOES images provide a context for out-of-field area of the TIRS scenes. The center square in the GOES image indicates the TIRS scene while the surrounding squares indicate approximately where the stray light source areas are for that scene. Recall that for the TIRS-only method, the edge pixel values are used as a substitute for the out-of-field area in the squares to the left and right of the TIRS scene. The TIRS-only method under-corrected the absolute error for the day 2013195 scene. Based on the context image (second image in Fig. 21), the edge pixel values are generally lower than the pixel values in the out-of-field area (i.e., the squares to the left and right of the scene). Since the edge pixel values are lower, the sampling algorithm would have calculated a smaller ghost signal to subtract from the original TIRS image. As such, the method under-corrected the stray light. For the day 2013275 scene, the TIRS-only method seemed to over-correct the absolute error. From the context image (third image in Fig. 21), it is clear that there was a cloud to the east of the scene that was not recorded by the edge pixels. Therefore the cold cloud could not be taken into account and the calculated ghost signal was higher than it should be, hence the over-correction.

These examples demonstrate the extent to which the TIRS-only correction method will be able to accurately correct the stray light from a TIRS scene. The method is expected to perform just as well as the wide-field sensor method for most scenes. However there will be cases in which the in-scene radiance (specifically the scene edge values) will not be representative of the out-of-field area to the west or east of the path. The most common occurrence will likely be clouds off-scene that cannot be accounted for.

C. Recommendation and Path Forward

The two stray light correction methods have advantages and disadvantages associated with them. The wide-field external sensor method is arguably the more accurate method since it incorporates coincident out-of-field data into the calculation of the stray light correction. However, the burden of obtaining wide-field data for every TIRS scene around Earth is a serious handicap that is not easily overcome. The alternative method of utilizing TIRS data itself to calculate the stray light correction was shown to perform as well as the wide-field sensor method in general. The deficiencies manifest themselves when the in-field radiance is not a good representation of the out-of-field radiance. Off-scene clouds will be the most common problem. Despite this deficiency,

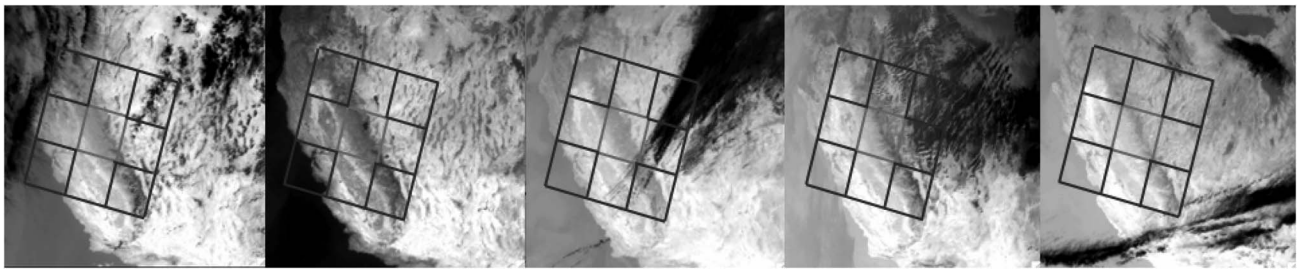

Fig. 21. Coincident GOES images to provide context for each of the five Lake Tahoe TIRS scenes from Fig. 20. The center square indicates the TIRS scene while the surrounding squares indicate the stray light source areas for the scene. White pixel values represent higher radiances (temperatures) than dark pixel values.

eliminating the need to obtain coincident wide-field data is a significant advantage.

The TIRS-only method was recommended to USGS/EROS for thorough testing in the hope that it will become the operational method for correcting the stray light in TIRS. At this time, EROS engineers are incorporating this method into the ground processing system for off-line testing. The system will allow for the production of many corrected scenes so that the regression coefficients can be refined if needed. It will also allow for the detailed characterization of the residual errors from the correction method. Additionally, since the sampling algorithm for the two proposed correction methods are identical, the option would still exist to produce a correction based on external sensor data. An off-line tool could be created so that a user requiring increased accuracy would be able to run the tool on external sensor data to generate a custom product utilizing the external sensor correction method.

6. SUMMARY

A stray light removal methodology was developed for the Landsat 8 Thermal Infrared Sensor that significantly enhances the thermal data both visually and radiometrically. To develop the algorithm suggested in this work, lunar scans were performed with the Landsat 8 observatory to identify stray light source regions. Due to the sparse nature of the maps created from these scans, an optical stray light model of the instrument was developed to more completely define the stray light source regions. The proposed algorithm involves the sampling of the out-of-field radiance surrounding a TIRS Earth scene at locations defined by the optical stray light maps for each detector. These out-of-field radiances are used to produce an estimated amount of ghost signal per detector through the developed regression process. The derived estimate of the ghost signal is then subtracted from the TIRS scene data to remove the stray light artifacts. Two potential data sources for the required out-of-field thermal infrared radiance are suggested: near-coincident external thermal infrared data (e.g., geostationary image data such as GOES) and the TIRS interval data itself. To train the algorithm, MODIS SST data were used to estimate TOA truth radiance and per-detector linear fits of TIRS/MODIS difference versus out-of-field radiance were found.

The algorithm presented here was tested on three different datasets: two scenes used to train the algorithm and one scene not used in the training. Several significant findings were observed in this analysis. First, nonuniform banding and striping that is present in the uncorrected TIRS data is significantly reduced upon applying the removal algorithm. As the methods presented here only supplement traditional calibration techniques, a final relative calibration must be performed to truly assess the impact of this algorithm against the final system requirements. However, convincing visual and quantitative evidence was presented (see Figs. 14–19) that demonstrates that the algorithm significantly reduced the banding artifacts in TIRS imagery. Additionally, although only measured for a handful of points, seasonal absolute calibration errors are reduced from over 9K to under 2K (Fig. 20).

Finally, the use of TIRS data as a surrogate for near-coincident external sensor data does not seem to hinder the performance of the stray light removal algorithm for the scenes presented here. This is extremely encouraging and represents a significant step toward the development of an operational stray light correction solution for the USGS Landsat ground processing system. Ongoing investigations are focused on quantifying the errors in the correction process. The major investigations include determining uncertainties in utilizing the MODIS SST due to temporal differences in the acquisition times between Landsat and MODIS; potentially refining the optical model stray light maps (directions and weights); refining the regression coefficients (α and β) to reduce regression fit errors over a large range of expected scene temperatures; and quantifying the impact of the assumption that TIRS data can be used to estimate incident ghost radiance (both due to the out-of-field land cover type and due to the presence of clouds in the out-of-field).

Goddard Space Flight Center (GSFC), National Aeronautics and Space Administration (NASA) (NNG09HP18C, NNX09AQ57A,NNX14AP40G).

REFERENCES

1. M. Montanaro, A. Lunsford, Z. Tesfaye, B. Wenny, and D. Reuter, "Radiometric calibration methodology of the Landsat 8 Thermal Infrared Sensor," Remote Sens. **6**, 8803–8821 (2014).
2. J. Barsi, J. Schott, S. Hook, N. Raqueno, B. Markham, and R. Radocinski, "Landsat-8 Thermal Infrared Sensor (TIRS) vicarious radiometric calibration," Remote Sens. **6**, 11607–11626 (2014).
3. M. Montanaro, A. Gerace, A. Lunsford, and D. Reuter, "Stray light artifacts in imagery from the Landsat 8 Thermal Infrared Sensor," Remote Sens. **6**, 10435–10456 (2014).
4. D. Reuter, C. Richardson, F. Pellerano, J. Irons, R. Allen, M. Anderson, M. Jhabvala, A. Lunsford, M. Montanaro, R. Smith, Z. Tesfaye, and K. Thome, "The Thermal Infrared Sensor (TIRS) on Landsat 8: design overview and pre-launch characterization," Remote Sens. **7**, 1135–1153 (2015).
5. D. Reuter, C. Richardson, J. Irons, R. Allen, M. Anderson, J. Budinoff, G. Casto, C. Coltharp, P. Finneran, B. Forsbacka, T. Hale, T. Jennings, M. Jhabvala, A. Lunsford, G. Magnuson, R. Mills, T. Morse, V. Otero, S. Rohrbach, R. Smith, T. Sullivan, Z. Tesfaye, K. Thome, G. Unger, and P. Whitehouse, "The Thermal Infrared Sensor on the Landsat data Continuity Mission," in *Proceedings of IEEE International Geoscience and Remote Sensing Symposium (IGARSS)* (IEEE, 2010), pp. 754–757.
6. United States Geological Survey, "Landsat 8," http://landsat.usgs.gov/landsat8.php, accessed Nov. 12, 2014.
7. United States Geological Survey, "Earth explorer," http://earthexplorer.usgs.gov/, accessed 12 Nov. 2014.
8. M. Montanaro, R. Levy, and B. Markham, "On-orbit radiometric performance of the Landsat 8 Thermal Infrared Sensor," Remote Sens. **6**, 11753–11769 (2014).
9. S. Hook, G. Chander, J. Barsi, R. Alley, A. Abtahi, F. Palluconi, B. Markham, R. Richards, S. Schladow, and D. Helder, "In-flight validation and recovery of water surface temperature with Landsat-5 thermal infrared data using an automated high-altitude lake validation site at Lake Tahoe," IEEE Trans. Geosci. Remote Sens. **42**, 2767–2776 (2004).
10. A. Berk, L. Bernstein, and D. Robertson, "MODTRAN: a moderate resolution model for LOWTRAN," http://www.dtic.mil/cgi-bin/GetTRDoc?Location=U2&doc=GetTRDoc.pdf&AD=ADA185384, accessed 10 Jan. 2015.
11. N. Mishra, M. Obaidul Haque, L. Leigh, D. Aaron, D. Helder, and B. Markham, "Radiometric cross calibration of Landsat 8 Operational Land Imager (OLI) and Landsat 7 Enhanced Thematic Mapper Plus (ETM+)," Remote Sens. **6**, 12619–12638 (2014).

12. ZEMAX Development Corporation, "Software for optical system design," http://www.zemax.com/, accessed 11 Jan. 2015.
13. NOAA Office of Satellite, and Product Operations, "Geostationary Operational Environmental Satellites (GOES)," http://www.ospo.noaa.gov/Operations/GOES/index.html, accessed 11 Jan. 2015.
14. Eumetsat, "Meteosat," http://www.eumetsat.int/website/home/Satellites/CurrentSatellites/Meteosat/index.html, accessed 11 Jan. 2015.
15. Meteorological Satellite Center (MSC) of JMA, "Himawari-8/9," http://www.data.jma.go.jp/mscweb/en/himawari89/, accessed 11 Jan. 2015.
16. O. Brown and P. Minnett, "MODIS infrared sea surface temperature algorithm algorithm theoretical basis document," http://modis.gsfc.nasa.gov/data/atbd/… atbd_mod25.pdf, accessed 11 Jan. 2015.
17. P. Minnett, O. Brown, R. Evans, E. Key, E. Kearns, K. Kilpatrick, A. Kumar, K. Maillet, and G. Szczodrak, "Sea-surface temperature measurements from the moderate-resolution imaging spectroradiometer (MODIS) on aqua and terra," in *Geoscience and Remote Sensing Symposium (IGARSS 2004)* (2004), Vol. **7**, pp. 4576–4579.
18. R. Gonzalez and R. Woods, "Morphological image processing," in *Digital Image Processing*, V. OBrien, ed. (Prentice, 2002), pp. 523–525.